APPLIED PHYSICS

Tuning moiré excitons in Janus heterobilayers for high-temperature Bose-Einstein condensation

Hongli Guo, Xu Zhang, Gang Lu*

Copyright © 2022 The Authors, some rights reserved; exclusive licensee American Association for the Advancement of Science. No claim to original U.S. Government Works. Distributed under a Creative Commons Attribution NonCommercial License 4.0 (CC BY-NC).

Using first-principles calculations, we predict that moiré excitons in twisted Janus heterobilayers could realize tunable and high-temperature Bose-Einstein condensation (BEC). The electric dipole in the Janus heterobilayers leads to charge-transfer interlayer and intralayer moiré excitons with exceptionally long lifetimes, in the absence of spacer layers. The electric dipole is also expected to enhance exciton-exciton repulsions at high exciton densities and can modulate moiré potentials that trap excitons for their condensation. The key parameters for exciton condensation, including exciton Bohr radius, binding energy, effective mass, and critical Mott density, are examined as a function of the twist angle. Last, exciton phase diagrams for the Janus heterobilayers are constructed from which one can estimate the BEC (>100 K) and superfluid (~30 K) transition temperatures. In addition to indirect interlayer excitons, we find that direct intralayer excitons can also condense at high temperatures, consistent with experiments.

INTRODUCTION

Two-dimensional (2D) moiré superlattices formed in van der Waals (vdW) heterostructures with a small angular or lattice mismatch have emerged as a fascinating and versatile platform to explore and engineer quantum states of matter. Driven by the interplay between flat energy bands and strong electron-electron interactions, fascinating quantum phenomena, such as unconventional superconductivity (*1*), charge density waves (*2*), and correlated insulating states [e.g., striped phases (*3*), Mott states (*4*, *5*), and Wigner crystals (*6*)] have been observed in the moiré superlattices. Recently, moiré superlattices in semiconducting transition metal dichalcogenides (TMDs) have garnered tremendous interest because they could host localized, long-lived, and valley-polarized moiré excitons (*7*–*10*), which are envisioned as single-photon emitters (*11*) in quantum information applications and as an essential element in excitonic devices (*12*).

Bose-Einstein condensation (BEC) is an exotic quantum state of matter where bosons, such as atoms, in a macroscopic system spontaneously condense into a single quantum state, leading to marked physical consequences, such as superfluidity (*13*). Since the first achievement of atomic BEC at nanokelvin temperatures (*14*), the quest to realize even higher BEC temperatures has fascinated physicists. Compared to atoms, excitons have much smaller masses and thus are expected to condense at much higher temperatures. Fogler *et al.* (*15*) are the first to predict that indirect or interlayer excitons in TMD bilayers could form BEC at ~100 K, and experimental evidence for high-temperature (~100 K) exciton condensation in $MoSe_2/WSe_2$ heterobilayers has recently been reported (*16*). In both cases, the BEC is formed by interlayer or indirect excitons whose electrons and holes are separated by hexagonal boron nitride spacer layers. The spatial separation of the electrons and the holes is deemed critical to achieve long-lived excitons necessary for BEC. Recent first-principles calculations (*17*) suggested that high-temperature BEC could also be realized in organic-TMD heterostructures in the absence of a spacer layer. This raises an intriguing question of whether moiré excitons in coupled TMD bilayers (i.e., without a spacer layer) could also condense at high temperatures and whether direct or intralayer moiré excitons with electrons and holes at the same TMD layer could realize high-temperature BEC. Note that localized moiré excitons have distinct optical selection rules and stronger correlations than the delocalized excitons examined in the previous works (*15*, *16*). In particular, moiré excitons can be readily tuned by the twist angle of the heterostructures. How the condensation of localized moiré excitons depends on the moiré superlattice or the twist angle is completely unknown. These are fascinating questions and, if answered, could have substantial impacts on the burgeoning field of excitonic BEC.

The excitonic BEC transition temperature T_c depends on several key factors: (i) the excitons should have longer lifetimes (>10 to 100 ns) than their thermalization times (~ps) (*18*); (ii) the exciton binding energy should be large enough, typically $>10k_BT_c$ (k_B is Boltzmann constant) (*15*, *16*); (iii) the presence of repulsive interactions between the excitons at high densities, which can stabilize the exciton condensate against the formation of competing exciton complexes; and (iv) the presence of potential traps that confine the exciton condensate. The last factor is of particular importance; breakthroughs in BEC were made possible by the realization of magneto-optical traps for atomic BEC (*14*, *19*) and in-plane potential traps for excitonic BEC in coupled semiconductor quantum wells (*20*, *21*).

Here, by means of first-principles calculations, we predict that moiré excitons in Janus TMD heterobilayers could realize tunable and high-temperature BEC. A Janus TMD monolayer consists of two distinct chalcogen atoms above and below the metal atom, producing an out-of-plane electric dipole. The electric dipole can yield charge-transfer intralayer or interlayer excitons, leading to exceptionally long exciton lifetimes (microseconds and milliseconds); the electric dipole can also enhance the repulsive interactions among the excitons. Both the intralayer and interlayer moiré excitons are predicted to have large binding energies (~0.40 eV), and they are trapped by deep moiré potentials, which are tunable by twist angle, strain, pressure, electric field, etc. (*11*, *22*–*24*) This is in sharp contrast to the coupled semiconductor quantum wells whose trap potentials are formed by random fluctuations of the quantum well thickness and the alloy disorder (*20*, *25*), which are difficult to control. The phase diagrams of the moiré excitons are constructed from

Department of Physics and Astronomy, California State University, Northridge, Northridge, CA 91330-8268, USA.
*Corresponding author. Email: gang.lu@csun.edu

Downloaded from https://www.science.org on December 19, 2025

which one can estimate the BEC (>100 K) and superfluid (~30 K) temperatures. We find that in addition to indirect interlayer excitons, direct intralayer excitons can also condense at high temperatures (123 to 193 K), in support of a recent experiment (*26*).

RESULTS

As shown in Fig. 1A, the top (or bottom) Te atoms in $MoTe_2$ monolayer are replaced by Se atoms to form a Janus monolayer MoSeTe (or MoTeSe). The Janus monolayers are then stacked with a WSe_2 monolayer to form vdW heterobilayers. Here, we focus on three twisted heterobilayers, including $WSe_2/MoTe_2$, WSe_2/MoTeSe, and WSe_2/MoSeTe, as shown in Fig. 2A. We then examine how excitonic properties may be tuned by the chemical modifications ($MoTe_2$ ➜ MoTeSe ➜ MoSeTe). Compared to other means of tuning [e.g., electric field, pressure, strain, and defects (*11*, *22*–*24*)], chemical tuning could have drastic effects yet received less attention.

Electric dipole and charge-transfer excitons in Janus monolayers

Owing to the asymmetry in the out-of-plane (or *z*) direction, Janus monolayer MoSeTe develops an electric dipole **P** as indicated by the purple arrow in Fig. 1A. The effect of the dipole is illustrated in Fig. 1B where the average electrostatic potentials along the *z* direction are plotted for both $MoTe_2$ and MoSeTe monolayers. The dipole yields an asymmetric electrostatic potential, manifested by the potential energy difference $\delta E = 0.7$ eV between the top and bottom vacuum of the Janus monolayer, as shown in Fig. 1C. In contrast, no such energy difference ($\delta E = 0$) exists in the $MoTe_2$ monolayer.

The electric dipole has important consequences on the excitonic properties. In Fig. 1D, we present the charge density of the lowest energy excitons in both monolayers. In $MoTe_2$, both the electron and the hole reside at the Mo layer because the conduction/valence edge states are contributed by the Mo d-orbitals. In MoSeTe, on the other hand, the dipole **P** drives the electron and the hole apart and the hole extends to the Se sublayer, forming a charge-transfer exciton. Thus, the wave function overlap between the electron and the hole is much smaller in MoSeTe, resulting in a dark exciton whose optical dipole is four orders of magnitude smaller than the corresponding bright exciton in $MoTe_2$. Therefore, the lowest exciton in Janus monolayer MoSeTe is expected to have a long lifetime, which is beneficial for BEC. Note that recent first-principles calculations predicted that charge-transfer interlayer excitons in organic/TMD heterostructures could condense at high temperatures (*17*). In this paper (and consistent with convention), we regard the excitons in the Janus monolayers as intralayer excitons despite their charge-transfer character. In contrast to conventional charge-transfer excitons that are formed between two distinct materials (i.e., donor and acceptor), the charge-transfer excitons in the Janus monolayers are in the same material.

Moiré potentials and flat bands in twisted Janus heterobilayers

We next examine the twisted heterobilayers. In Fig. 2 (A and B), we display the atomic structures and the band alignments of the three heterobilayers with a twist angle $\theta = 30°$. The first two heterobilayers exhibit the type I band alignment, while the third one has the type II band alignment. Note that the last two heterobilayers have the identical chemical composition but with the bottom Janus monolayer flipped upside down. Thus, the electric dipole in the Janus monolayer is reversed between the two (fig. S1), switching the band alignment from type I in WSe_2/MoTeSe to type II in WSe_2/MoSeTe.

To facilitate exciton condensation, it is highly desirable to create in-plane potentials to trap excitons; this can be achieved by moiré potentials in twisted heterobilayers. Moreover, one can modulate the magnitude of the moiré potential by changing the twist angle. In the following, we consider twisted heterobilayers with a small twist angle $\theta = 0.22°$, which is expected to result in deeper moiré potentials. In Fig. 2G, we show the relaxed moiré supercell for WSe_2/MoTeSe heterobilayer ($\theta = 0.22°$) with 1356 atoms. On the basis of the relaxed structure, we can estimate the moiré potential as the bandgap variation $\delta E_g = E_g - \langle E_g \rangle$ of the supercell; $\langle E_g \rangle$ is the average

Downloaded from https://www.science.org on December 19, 2025

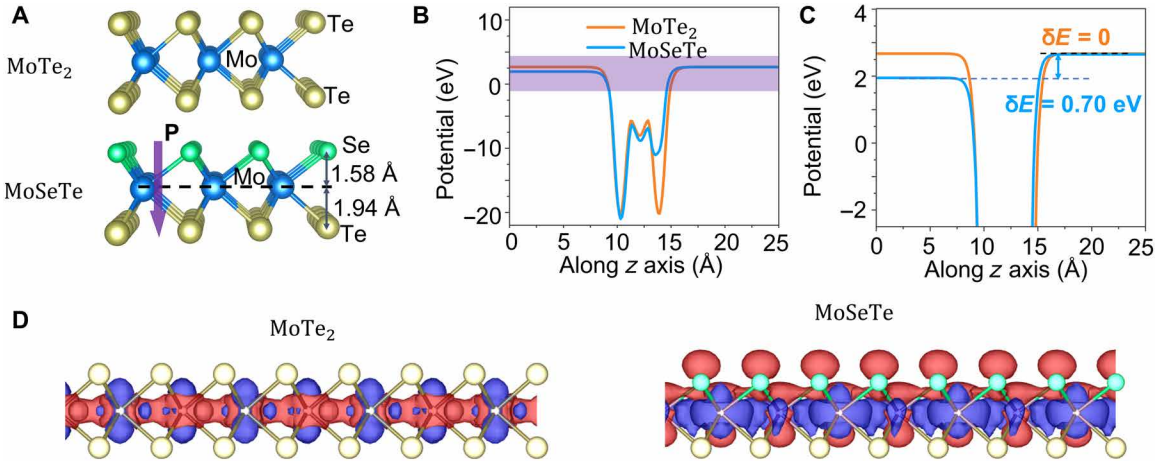

Fig. 1. Electric dipole and charge-transfer exciton in Janus MoSeTe monolayer. (**A**) Atomic structures of $MoTe_2$ and Janus MoSeTe monolayer. The distances between Se, Mo, and Te sublayers are indicated. The purple arrow represents the electric dipole **P** in Janus MoSeTe monolayer. (**B**) The average electrostatic potential energy along the *z* axis of $MoTe_2$ and MoSeTe monolayer. (**C**) The blown-up view of shaded region in (B), showing the potential energy difference ($\delta E = 0.7$ eV) between the top and bottom vacuum in MoSeTe. (**D**) Charge densities of the lowest energy excitons in $MoTe_2$ (left) and MoSeTe monolayer (right). The blue (red) color represents the charge density of the electron (hole) of the exciton. The isosurface value is set at 10^{-4} e/Å^3.

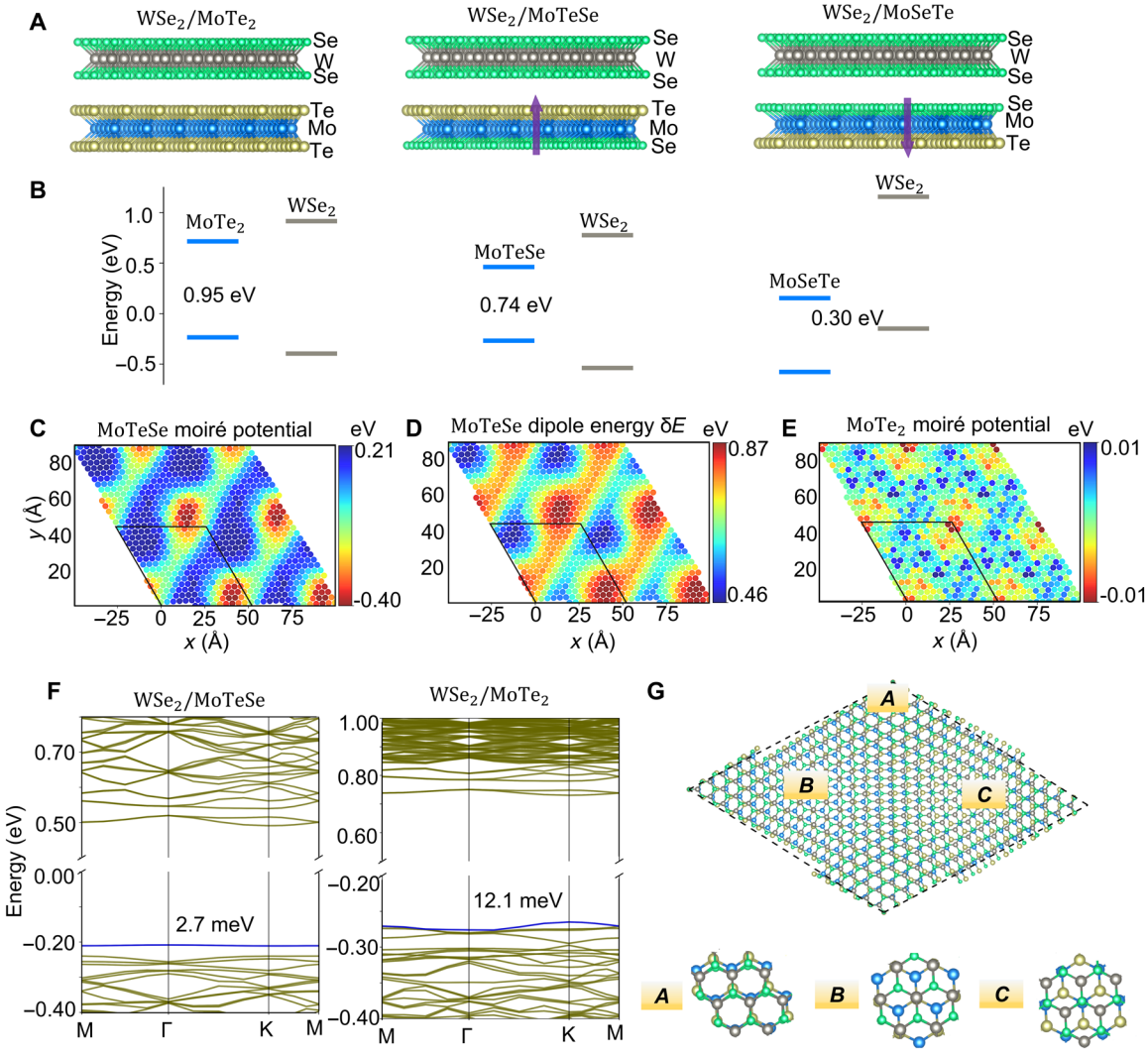

Fig. 2. Band alignment, moiré potential, and flat band in Janus heterobilayers. (**A**) Schematic pictures of the three twisted heterobilayers $WSe_2/MoTe_2$, WSe_2/MoTeSe, and WSe_2/MoSeTe (θ = 30°). (**B**) The band alignment diagrams of the three heterobilayers; the bandgaps of the heterostructures are also indicated. (**C**) The moiré potential for the relaxed MoTeSe layer in twisted WSe_2/MoTeSe heterobilayer (θ = 0.22°). (**D**) The dipole potential energy (δ*E*) for the relaxed MoTeSe layer in twisted WSe_2/MoTeSe heterobilayer (θ = 0.22°). (**E**) The moiré potential for the relaxed $MoTe_2$ layer in twisted $WSe_2/MoTe_2$ heterobilayer (θ = 0.22°). (**F**) The single-particle band structure of twisted WSe_2/MoTeSe and $WSe_2/MoTe_2$ bilayer (θ = 0.22°). The blue line represents the top valence band with a bandwidth of 2.7 and 12.1 meV, respectively. (**G**) The computational unit cell for the moiré superlattice of twisted WSe_2/MoTeSe heterobilayer (θ = 0.22°). Three high-symmetry points (*A*, *B*, and *C*) in the supercell are labeled, and their stacking structures are shown below.

value of the bandgap E_g (the computation detail for the moiré potential can be found in the Supplementary Materials). As shown in Fig. 2 (C and E), a much deeper moiré potential (0.61 eV) is formed in WSe_2/MoTeSe as compared to that in $WSe_2/MoTe_2$ (0.02 eV). The deep and tunable moiré potentials in Janus heterobilayers could provide more robust and controllable traps for exciton condensation than those in the coupled semiconductor quantum wells.

To shed light on the contrasting moiré potentials between WSe_2/MoTeSe and $WSe_2/MoTe_2$, we determine the spatial distribution of δ*E*, which represents the dipole energy distribution in WSe_2/MoTeSe superlattice. As shown in Fig. 2D, there is a strong resemblance between the distribution of δ*E* and the distribution of δE_g in WSe_2/MoTeSe, suggesting a connection between the dipole and the moiré potential. The connection is also apparent in $WSe_2/MoTe_2$, where the negligible moiré potential is consistent with the absence of the dipole (δ*E* = 0). Hence, the deep moiré potential in WSe_2/MoTeSe can be attributed to the dipole in the Janus monolayer. Another important consequence of the deep moiré potential is the formation of an isolated flat valence band (2.7 meV) in WSe_2/MoTeSe, as shown in Fig. 2F. The flat band implies small kinetic energy of the hole (and exciton), which could benefit the trapping and condensation of the excitons. A less flat valence band is also observed in twisted $WSe_2/MoTe_2$ and WSe_2/MoSeTe (fig. S3). The moiré bands in $WSe_2/MoTe_2$ heterobilayers have recently been shown to yield finite Chern numbers due to the lattice relaxation (*27*).

Tuning moiré exciton lifetimes

Exciton lifetime is one of the most important factors for BEC. In the following, we first explore chemical tuning of exciton lifetime. To this end, we compare the lifetimes of the lowest moiré excitons in

Downloaded from https://www.science.org on December 19, 2025

$WSe_2/MoTe_2$, $WSe_2/MoTeSe$, and $WSe_2/MoSeTe$ heterobilayers with the same twist angle (θ = 30°). As shown in Fig. 3A, because $WSe_2/MoTe_2$ and $WSe_2/MoTeSe$ have a type I band alignment, their lowest excitations are intralayer or direct excitons with the electrons and holes residing at the same monolayer ($MoTe_2$ or MoTeSe); no electron or hole is at WSe_2 layer because of its wider bandgap (Fig. 2B). The intralayer exciton in $WSe_2/MoTeSe$ has the charge-transfer character due to the electric dipole in MoTeSe as mentioned before. $WSe_2/MoSeTe$, on the other hand, has a type II band alignment, and its lowest energy exciton has an interlayer character with the electron and hole separated at different monolayers. The spatial separation of the electron and the hole renders the interlayer exciton dark, whose optical dipole is three (or two) orders of magnitude smaller than that of the intralayer exciton in $WSe_2/MoTe_2$ (or $WSe_2/MoTeSe$). The charge-transfer character yields a smaller optical dipole for the intralayer exciton in $WSe_2/MoTeSe$ as compared to the intralayer exciton in $WSe_2/MoTe_2$. The radiative lifetimes of the excitons exhibit the opposite trends as the optical dipoles. The intralayer exciton in $WSe_2/MoTe_2$ has the shortest lifetime of τ_0 = 145 fs, while the intralayer exciton in $WSe_2/MoTeSe$ has a much longer lifetime of τ_0 = 23.7 ns. The interlayer exciton in $WSe_2/MoSeTe$ is predicted to have an exceptionally long lifetime $\tau_0 \sim 2$ μs. Previous first-principles GW-Bethe–Salpeter equation calculations have also reported similarly long lifetimes for dark excitons in TMD monolayers and heterobilayers, ranging from a few microseconds to milliseconds (*28*). It is generally believed that BEC should be possible if the exciton lifetime is longer than 10 to 100 ns (*18*); thus, both the charge-transfer intralayer exciton in $WSe_2/MoTeSe$ and the interlayer exciton in $WSe_2/MoSeTe$ could realize BEC, and we will estimate their transition temperatures in the next section.

Next, we examine exciton lifetime as a function of the twist angle. Specifically, we focus on the lowest intralayer exciton in $WSe_2/MoTe_2$ by considering six twist angles (θ = 0.22°, 1.93°, 10.58°, 30°, 48.07°, and 58.07°). Note that the moiré supercell with θ = 1.93° (or 10.58°) has the same lattice parameters as that with θ = 58.07° (or 48.07°). In Fig. 3B, we present the optical dipole and the radiative lifetime of the exciton as a function of the twist angle. The optical dipole increases with the twist angle until θ = 30° and then decreases. The radiative lifetime follows the opposite trend. Thus, to increase the exciton lifetime in $WSe_2/MoTe_2$, one should tune the twist angle to be near either 0° or 60°. For example, for θ = 0.22°, the lifetime of the intralayer exciton in $WSe_2/MoTe_2$ could reach ~100 ns (this amounts to six orders of magnitude increase in the lifetime from θ = 30°), rendering it possible for BEC. In Fig. 3C, we display the charge density of the intralayer exciton in $WSe_2/MoTe_2$ with θ = 0.22° and θ = 30°. The electron and hole are much more separated in the former (θ = 0.22°) than in the latter (θ = 30°); hence, the exciton has a much longer lifetime in the former. The exciton lifetimes in $WSe_2/MoTeSe$ and $WSe_2/MoSeTe$ follow the similar twist angle dependence. In particular, for θ = 0.22°, we calculate the lifetime of the

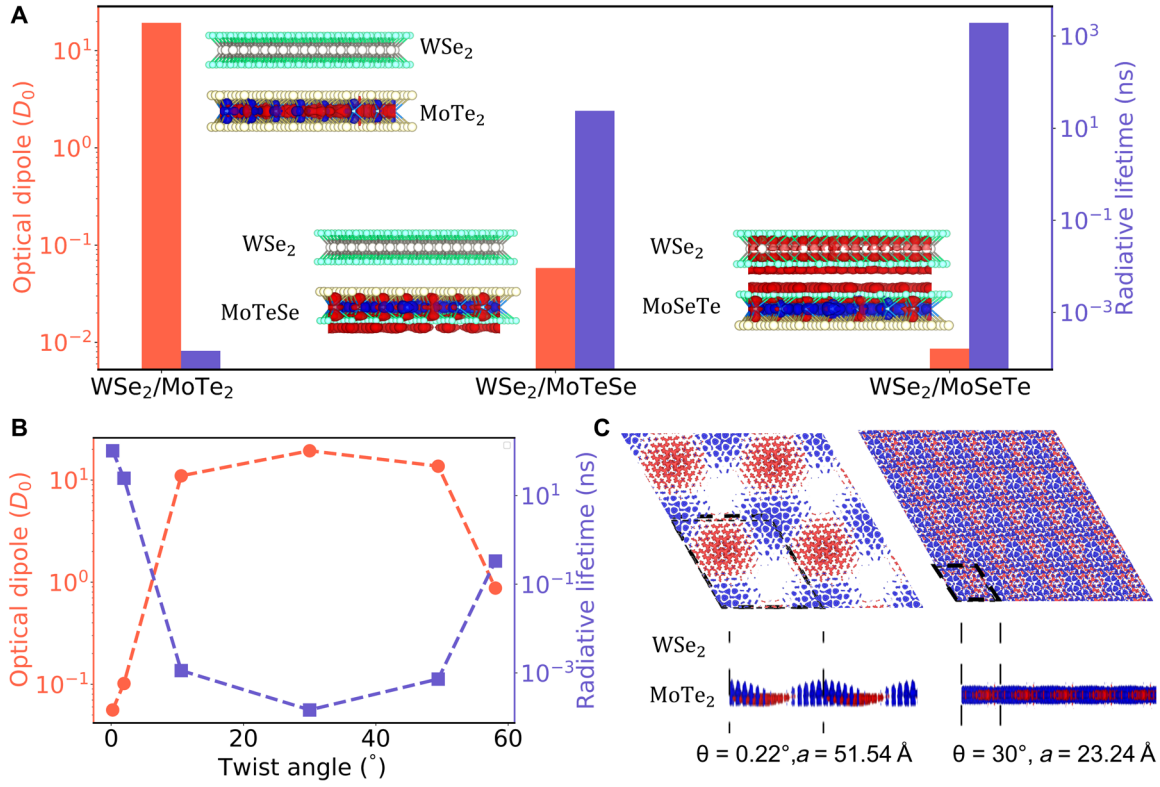

Fig. 3. Tunable moiré exciton lifetimes in heterobilayers. (**A**) Optical dipole moment (left), radiative lifetime (right), and charge density (inset) of the lowest energy excitons in twisted $WSe_2/MoTe_2$, $WSe_2/MoTeSe$, and $WSe_2/MoSeTe$ heterobilayers (θ = 30°). (**B**) Optical dipole moment (red) and radiative lifetime (blue) of the lowest intralayer exciton in twisted $WSe_2/MoTe_2$ bilayer as a function of the twist angle. (**C**) The top and side views of the charge densities for the lowest intralayer excitons in $WSe_2/MoTe_2$ with θ = 0.22° and 30°. The blue (red) color represents the charge density of the electron (hole). The unit cell of the moiré superlattice is indicated by the black dashed box (a is the lattice constant). All isosurface values are set at 10^{-4} e/Å^3.

Downloaded from https://www.science.org on December 19, 2025

intralayer exciton in WSe_2/MoTeSe as ~1.87 μs, and the lifetime of the interlayer exciton in WSe_2/MoSeTe can reach ~3 ms. These are exceptionally long lifetimes, making these moiré excitons highly promising for BEC. We emphasize that these exceptionally long lifetimes are realized in the absence of a spacer layer in the heterostructures.

BEC temperature of moiré excitons

In this section, we examine the exciton phase diagram and estimate BEC and superfluid transition temperatures in the three heterostructures, following an approach proposed by Fogler *et al.* (*15*). As shown in the phase diagram (Fig. 4A), four competing phases, including classical exciton gas, classical electron-hole gas, degenerate exciton Bose gas, and degenerate electron-hole Fermi gas are possible as a function of temperature (T) and exciton density (n). The phases are divided by two lines: a blue vertical line that separates the exciton gases from the electron-hole gases at the critical Mott density n_c and a red sloped line that separates the classical gases from the degenerate Fermi or Bose gases. BEC takes place below the critical Mott density and under the degenerate temperature (red line), which depends on the exciton density n. Hence, the BEC transition temperature (T_c) is where the two lines cross.

The critical Mott density n_c can be determined by the exciton Bohr radius R via $n_c \approx \frac{1}{\pi R^2}$ (*15*, *17*, *29*, *30*). Here, we estimate the exciton Bohr radius R by the root mean square (RMS) radius of the exciton wave function defined as (*17*)

$$R^2 = \langle \mathrm{RMS} \rangle = \frac{\int |r - r_0|^2 \rho(r)\, dr}{\int \rho(r)\, dr}$$

Here, $\rho(r)$ is the square modulus for the electronic part of the excitonic wave function; r_0 denotes the center of the electron distribution with the hole fixed at the corner of the moiré supercell. The electronic part of the excitonic wave function for the lowest intralayer exciton in WSe_2/MoTeSe ($\theta = 0.22°$) is shown in Fig. 4B, where the hole is indicated by the red cross. The Bohr radius R is estimated as 1.61 nm, yielding a critical Mott density $n_c = 1.23 \times 10^{13}\ \mathrm{cm}^{-2}$, which sets the high-density limit for BEC in WSe_2/MoTeSe ($\theta = 0.22°$). As a comparison, the exciton density in $MoSe_2/WSe_2$ heterobilayers where the experimental evidence for exciton condensation was observed (*16*) is in the order of $10^{12}\ \mathrm{cm}^{-2}$.

The degeneracy temperature (T_d) at which the classical gases cross over to the degenerate Bose or Fermi gases is given by $k_B T_d = \frac{2\pi\hbar^2}{M} n$, as shown by the red line. Here, M is the effective mass of the exciton and can be estimated as the sum of the electron and hole effective masses. In fig. S4, we display the relative contributions of various electron-hole transitions for the lowest intralayer exciton in WSe_2/MoTeSe ($\theta = 0.22°$). We find that the lowest exciton comprises primarily the transition from the valence band maximum (VBM) to the conduction band minimum (CBM); thus, M is the sum of the effective masses of the electron in CBM and the hole in VBM. Last, the BEC transition temperature (T_c) is the degeneracy temperature at the critical Mott density n_c. For the lowest intralayer exciton in WSe_2/MoTeSe ($\theta = 0.22°$), T_c is estimated as 128 K. Therefore, we predict that the intralayer or direct excitons in twisted WSe_2/MoTeSe heterobilayers could condense at high temperatures. Our prediction is consistent with a recent experiment that has shown evidence of high-temperature (~150 K) condensation of intralayer excitons in

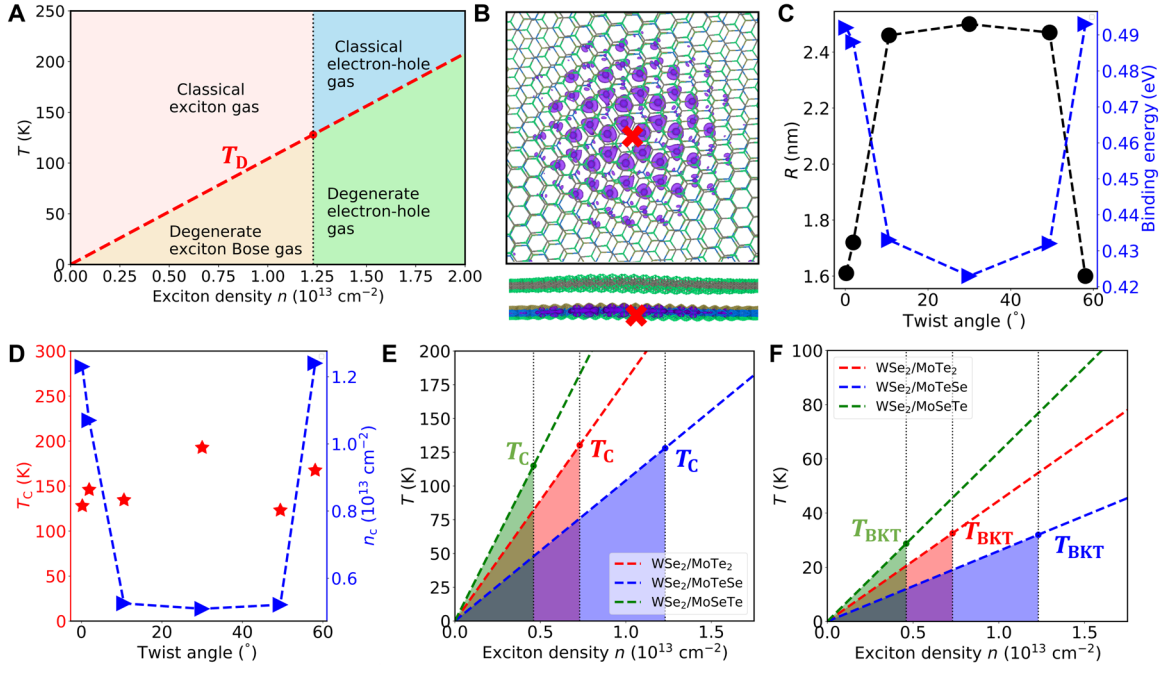

Fig. 4. BEC phase diagram of moiré excitons. (**A**) Phase diagram for the lowest intralayer moiré exciton in WSe_2/MoSeTe bilayer ($\theta = 0.22°$) as a function of the exciton density n and temperature T. (**B**) The top and side view for the electronic part of the excitonic wave function for the lowest intralayer exciton in WSe_2/MoTeSe bilayer ($\theta = 0.22°$); the hole is fixed at the red cross. (**C**) The Bohr radius R (black line) and the binding energy (blue line) of the lowest intralayer exciton in twisted WSe_2/MoTeSe bilayer as a function of the twist angle. (**D**) The BEC transition temperature T_c (red star) and the critical Mott density n_c (blue triangle) for the lowest intralayer exciton in twisted WSe_2/MoTeSe heterobilayer as a function of the twist angle. (**E**) The BEC portion of the phase diagram and (**F**) Berezinskii-Kosterlitz-Thouless (BKT) superfluid transition for the lowest intralayer exciton in twisted $WSe_2/MoTe_2$ (red), WSe_2/MoTeSe (blue), and WSe_2/MoSeTe (green) heterobilayer ($\theta = 0.22°$).

Downloaded from https://www.science.org on December 19, 2025

monolayer MoS_2 (*26*). The intralayer excitons in monolayer MoS_2 are delocalized with much shorter lifetimes, as compared to the localized moiré excitons in WSe_2/MoTeSe heterobilayers. One would thus expect that the intralayer moiré excitons could condense at a higher temperature. The high-temperature condensation in the experiment was attributed to strong repulsions among the excitons in MoS_2 (*26*). Thus, the built-in dipoles in the Janus bilayers could also play an important role in the condensation of moiré excitons.

To illustrate the dependence of BEC on the twist angle, we calculate the Bohr radius (R), exciton effective mass (M), exciton binding energy, and degeneracy temperature (T_d) for the intralayer excitons in WSe_2/MoTeSe as a function of the twist angle θ. As shown in Fig. 4C, the exciton Bohr radius is strongly correlated to its binding energy. As the twist angle approaches 0° or 60°, the moiré potential becomes deeper, and the exciton becomes more localized with a larger binding energy and a smaller Bohr radius. Similarly, a deeper moiré potential results in flatter (or less dispersive) bands and, thus, greater effective masses for the exciton, as shown in table S1. In Fig. 4D, we display the dependence of n_c and T_c on the twist angle, and it is found that n_c increases as θ approaches 0° or 60°, and T_c is tunable from 123 to 193 K.

We have also carried out similar calculations for the two other heterobilayers (WSe_2/$MoTe_2$ and WSe_2/MoSeTe with θ = 0.22°), and the results are summarized in Fig. 4E. The lowest intralayer exciton in WSe_2/$MoTe_2$ and the lowest interlayer exciton in WSe_2/MoSeTe are considered. The BEC temperature for the intralayer exciton in WSe_2/$MoTe_2$ is estimated as 130 K, and the interlayer exciton in WSe_2/MoSeTe is estimated as 115 K. Last, the 2D excitons can also transform into a superfluid state via the Berezinskii-Kosterlitz-Thouless (BKT) transition below a critical temperature (*15*) given by $k_B T_{BKT} = \frac{\pi\hbar^2}{2M} n$. In Fig. 4 (E and F), we summarize T_{BKT} dependence on the exciton density for the three twisted heterobilayers (θ = 0.22°). The predicted superfluid temperature is ~30 K for the three heterostructures.

In this work, we focused on the radiative recombination of excitons, but phonon-assisted nonradiative recombination should also be considered. According to previous theoretical calculations and experiments, the nonradiative lifetimes of excitons in TMDs are in the order of nanoseconds (*31*–*33*), which are sufficiently long for BEC (*18*). Furthermore, the nonradiative recombination rates depend on nonadiabatic coupling (NAC) between relevant conduction and valence bands *(34)*, and NAC is determined primarily by the wave function overlap between these bands. As shown in Fig. 3C, the electron and the hole of the lowest exciton in twisted moiré superlattice (θ = 0.22°) are well separated with little spatial overlap; thus, NAC is expected to be exceedingly small, leading to long nonradiative lifetimes in the moiré bilayers. Similarly, Auger-like processes are not believed to be important because only the lowest energy excitons are likely to be involved in BEC. On the other hand, the electric dipole in the Janus heterolayers is expected to modify the Coulomb interaction between the electron and the hole in the excitons, which, in turn, could affect their condensation. The present time-dependent density functional theory with optimally tuned, screened, and range-separated hybrid exchange-correlation functionals is capable of capturing the Coulomb interaction (see Methods). Thus, the exciton lifetime, binding energy, Bohr radius, and effective mass in the presence of the electric dipole can be correctly described in our first-principles calculations. However, commonly used theoretical models for exciton condensation, such as that of Fogler *et al.* (*15*, *17*, *29*) do not consider exciton trapping by either moiré or other potentials nor is exciton-exciton repulsion included in these models. To remedy these deficiencies, we further adopt a two-fluid mean-field model (*35*, *36*) to refine our predictions. In this model, the condensate wave function is described by Gross-Pitaevskii equation in which both a trapping potential and a repulsive interaction between excitons are considered. The kinetic energy of the moiré excitons can be ignored (Thomas-Fermi approximation) thanks to the flat exciton energy bands (see Methods for details). On the basis of this model, we can determine the BEC transition temperatures T_c as a function of the moiré exciton density n. For the lowest intralayer exciton in MoTeSe/WSe_2 bilayer (θ = 0.22°), T_c is estimated as 144 K for $n_c = 1.23 \times 10^{13}\text{cm}^{-2}$; this is slightly higher than the temperature (128 K) obtained from the model of Fogler *et al.* Additional results from the two-fluid model can be found in the Supplementary Materials (figs. S6 and S7).

DISCUSSION

Because of their light masses and high binding energies, excitons in 2D semiconductors are expected to condense at higher temperatures. In this work, by means of first-principles calculations, we predict that both direct and indirect moiré excitons in twisted Janus heterobilayers could realize tunable high-temperature BEC and superfluid transitions. Two unique features that render the Janus heterobilayers particularly attractive are the formation of deep moiré potentials and the presence of out-of-plane electric dipoles. The former can provide potential traps necessary for exciton condensation. The availability of deep tunable trap potentials is the most distinctive advantage of the Janus heterobilayers for exciton condensation. The electric dipoles in the Janus bilayers, on the other hand, can enhance exciton-exciton repulsions, which are critical for BEC when the exciton density is high. The out-of-plane electric dipoles are particularly important to intralayer excitons whose in-plane interactions are normally weak. As suggested in the recent experiment (*26*), strong exciton-exciton repulsions are the driving force for high-temperature condensation of intralayer excitons in monolayer MoS_2. The electric dipoles also lead to charge-transfer moiré excitons with exceptionally long lifetimes (up to milliseconds) that are tunable by the twist angle. The electric dipoles are found to be responsible for the deep moiré potentials in the Janus heterobilayers, which, in turn, yield isolated flat bands. Both interlayer and intralayer moiré excitons are predicted to have large binding energies (~0.40 eV), which is necessary for high-temperature BEC (*15*, *16*). The key parameters for exciton condensation, including exciton Bohr radius, binding energy, effective mass, and critical Mott density are examined as a function of the twist angle in WSe_2/MoTeSe heterobilayer for the intralayer exciton. Last, the exciton phase diagrams are constructed from which one can estimate the BEC (>100 K) and superfluid (~30 K) transition temperatures. We find that the direct intralayer excitons in WSe_2/MoTeSe heterobilayers can condense at high temperatures (123 to 193 K), in support of the recent experiment (*26*). Our work lays the foundation for future experimental exploration of moiré excitons for tunable and high-temperature BEC.

METHODS

First-principles ground state calculations

The ground state properties, including single-particle band structures and optimized atomic structures of various heterobilayers examined in

Downloaded from https://www.science.org on December 19, 2025

this work were determined using Vienna Ab initio Simulation Package (*37*, *38*). The Perdew-Burke-Ernzerhof exchange-correlation functional (*39*) along with projector-augmented wave potentials (*40*) was used in these calculations. The vdW interaction was considered via vdW-D2 functional (*41*). For the band alignment diagrams shown in Fig. 2B, spin-orbit coupling was included in the calculations. To determine the band structures of the moiré superlattices with $\theta = 0.22°$, five special k-points were sampled along each of the high symmetry directions in the Brillouin zone. The atomic geometry in each moiré superlattice was fully optimized until the residual force on each atom was less than 0.01 eV $Å^{-1}$. A 20 Å vacuum layer was included in the supercells to separate the periodic images.

First-principles excited state calculations

To determine the energies and the many-body wave functions of the excitons in the heterobilayers, we used a recently developed first-principles approach based on linear-response time-dependent density functional theory (LR-TDDFT) (*42*, *43*) with optimally tuned, screened, and range-separated hybrid (OT-SRSH) exchange-correlation functionals (*22*, *24*, *44*–*47*). Unlike the traditional LR-TDDFT method with local and semilocal functionals, the TDDFT method using the OT-SRSH functionals can capture the correct long-range electron-electron and electron-hole interactions in solids by choosing appropriate parameters (*48*–*52*). The LR-TDDFT methods with hybrid exchange-correlation functionals have been used extensively to study optical and excitonic properties in solids; see, for example, (*53*–*55*) and references therein, in addition to (*48*–*52*). In this work, we solve the following non-Hermitian eigenvalue equations of Casida (*56*) to determine the excitation energies ω_I

$$\begin{pmatrix} A & B \\ B^* & A^* \end{pmatrix}\begin{pmatrix} X_I \\ Y_I \end{pmatrix} = \omega_I \begin{pmatrix} 1 & 0 \\ 0 & -1 \end{pmatrix}\begin{pmatrix} X_I \\ Y_I \end{pmatrix} \quad (1)$$

where the pseudo-eigenvalue ω_I is the Ith exciton energy level and $X_{I,ij}$ and $Y_{I,ij}$ are eigenvectors, which are used to determine the exciton wave functions. The matrix elements of A and B based on Kohn-Sham (KS) orbitals ($ij\sigma$) are given by

$$A_{ij\sigma,kl\tau} = \delta_{i,k}\delta_{j,l}\delta_{\sigma,\tau}(\varepsilon_{j\sigma} - \varepsilon_{i\sigma}) + K_{ij\sigma,kl\tau} \quad (2)$$

$$B_{ij\sigma,kl\tau} = K_{ij\sigma,lk\tau} \quad (3)$$

Here, $K_{ij\sigma,lk\tau}$ is the coupling matrix whose indices i and k indicate the occupied KS orbitals, and j and l represent the virtual KS orbitals (*57*). Following the assignment ansatz of Casida (*56*), the many-body wave function of the excited state I can be written as

$$\Phi_I \approx \sum_{ij\sigma}\frac{X_{I,ij\sigma} + Y_{I,ij\sigma}}{\sqrt{\omega_I}} a^\dagger{}_{j\sigma} a_{i\sigma}\Phi_0 = \sum_{ij\sigma} Z_{I,ij} a^\dagger{}_{j\sigma} a_{i\sigma}\Phi_0 \quad (4)$$

where $z_{I,ij} = (X_{I,ij} + Y_{I,ij})/\sqrt{\omega_I}$. $a_{i\sigma}$ ($a^\dagger_{i\sigma}$) is the annihilation (creation) operator acting on the ith KS orbital with spin σ and Φ_0 is the ground state many-body wave function taken as the single Slater determinant of the occupied KS orbitals.

In the TDDFT-OT-SRSH method, there are three parameters—α, β, and γ—needed to be specified. α controls the short-range exact exchange, and β is chosen to satisfy the requirement $\alpha + \beta = 1/\varepsilon$, where ε is the scalar dielectric constant. The optimal set of the parameters ($\alpha = 0.025$, $\beta = 0.975$, and $\gamma = 0.03$) was determined by fitting the quasiparticle gap of nontwist $WSe_2/MoTe_2$ bilayer from the DFT-OT-SRSH calculations to that from the GW calculations. This is a typical procedure used in TDDFT-OT-SRSH calculations (*48*–*52*). With this set of parameters, we obtained an optical gap of 1.13 and 1.09 eV for $WSe_2/MoTe_2$ heterobilayer and $MoTe_2$ monolayer, respectively, which agrees well to experimental results (*49*, *58*–*60*). The exciton binding energy E_b defined as the difference between the quasiparticle gap and the optical gap is calculated as 0.49 and 0.51 eV, respectively, which is also in reasonable agreement with previous results (0.58± 0.08 eV) (*60*) for the intralayer exciton in $MoTe_2$ monolayer. To further validate our method, we compute the exciton charge density and the electronic part of the excitonic wave function for the lowest intralayer moiré exciton in the angle-aligned WS_2/WSe_2 heterobilayer (the moiré superlattice is formed owing to the lattice mismatch of the layers). The results shown in fig. S5 agree very well to those obtained from GW-BSE calculations (*61*). Additional validations of the method can be found in previous publications on various 2D materials and their heterostructures (*22*, *24*, *44*, *46*). Last, as very large supercells are used in the TDDFT calculations for the moiré excitons, only the Γ point of the Brillouin zone is sampled. Thus, the exciton momentum is zero.

The optical dipole moment calculations

To determine the optical dipole moment for each moiré exciton, we first examine the electron-hole transitions involved in the exciton. As mentioned above, the many-body wave function of the exciton Φ_I is expressed as a linear combination of electron-hole transitions, and $Z_{I,ij}$ represents the corresponding electron-hole transition amplitude. The optical dipole moment (μ_I) of the exciton I is calculated as

$$\mu_I = \sum_{ij} Z_{I,ij} p_{ij}$$

$$p_{ij} = \langle \varphi_i | e\mathbf{r} | \varphi_j \rangle$$

where p_{ij} is the transition dipole moment between the KS occupied state φ_i and unoccupied state φ_j. e is the electron charge, and $\mathbf{r}$ is the position operator of the electron.

The exciton radiative lifetime calculations

As only the Γ point is used in the calculations of excitonic properties with large moiré supercells, the radiative recombination rate of an exciton is given by (*62*)

$$\gamma_I = \frac{e^2 \omega_I {\mu_I}^2}{\epsilon_0 \hbar^2 c A_{uc}}$$

Here, A_{uc} is the area of the in-plane unit cell, e is the electron charge, ω_I is the exciton energy, and μ_I is the optical dipole moment. ϵ_0 is the vacuum permittivity, and c is the speed of light. The radiative lifetime of the exciton is given as

$$\tau_0 = {\gamma_I}^{-1}$$

The two-fluid mean-field BEC model

In this model, the BEC condensate wave function $\psi(r)$ is described by the Gross-Pitaevskii equation below

$$-\frac{\hbar^2}{2m}\nabla^2\psi(r) + V(r)\psi(r) + 2g n_1(r)\psi(r) + g\psi^3(r) = \mu\psi(r) \quad (5)$$

Downloaded from https://www.science.org on December 19, 2025

where g represents the interaction strength of exciton-exciton repulsion and $V(r)$ represents the moiré potential. $n_1(r)$ is the distribution function of noncondensed excitons, and μ is the chemical potential determined by the equilibrium of the condensed and noncondensed excitons. In the model, the periodic moiré potential takes the form $V(r) = 2V\sum_{j=1,3,5}\cos(\mathbf{b}_j \cdot \mathbf{r} - \varphi)$ (*10*), where $\mathbf{b}_j$ are the moiré reciprocal lattice vectors and φ is a phase that specifies the potential extrema. Near the potential center, the potential is assumed to be harmonic, i.e., $V(r) = \frac{1}{2}m\omega^2 r^2$, where $\hbar\omega$ denotes the average spacing of the quantized energy spectrum of the moiré excitons (*10*). For the intralayer moiré exciton in MoTeSe/WSe_2 Janus bilayer (θ = 0.22°), we obtain $\hbar\omega$ = 10 meV, which is similar to the value reported in (*10*). Here, g represents strength of the exciton-exciton repulson, which can be approximated as $E_{\text{repul}} = \frac{ne^2d}{\varepsilon} = gn$ (*12*); thus, $g = \frac{e^2d}{\varepsilon}$, where n is the exciton density, d is the size of the electric-hole dipole, and ε is the dielectric constant (~5.2). d can be approximated by the distance between the electron and the hole (~3 Å) in the Janus monolayer. Hence, we arrive at g = 1.09 a. u. = 3.1 meV · a^2 (a = 5.14 nm).

In Eq. 5, the kinetic energy of the moiré excitons can be ignored (Thomas-Fermi approximation) owing to the flat exciton bands. The Thomas-Fermi approximation is also used by others in the two-fluid model (*35*, *36*). Here, we define $N_0 = \int \psi^2(r)d^2r$ as the number of condensed excitons, and N is the total number of excitons, including both condensed (N_0) and noncondensed excitons. Following the approach in (*35*), we can obtain the following equations

$$\psi^2(r) = \frac{1}{g}[\mu - V(r) - 2gn_1(r)]\theta(\mu - V(r) - 2gn_1(r))$$

$$N_0 = \int\psi^2(r)\,d^2r = \frac{\pi\hbar^2}{gm}\left(\frac{\mu}{\hbar\omega}\right)^2$$

and

$$N = N_0 + \left(\frac{k_B T}{\hbar\omega}\right)^2\left[\frac{\pi^2}{3} - \text{dilog}(1 - e^{\frac{\mu}{k_B T}})\right]$$

These equations can be solved self-consistently to determine T_c and other relevant quantities. More specifically, T_c is defined as the critical temperature below which the exciton condensation begins (i.e., $N_0 = 0$). The solution of the above equations depends on the exciton density $n = N/A$ (A is the area of the 2D system). The results of T_c are shown in fig. S6, and the temperature dependence of condensation fraction is shown in fig. S7.

SUPPLEMENTARY MATERIALS

Supplementary material for this article is available at https://science.org/doi/10.1126/sciadv.abp9757

REFERENCES AND NOTES

1. Y. Cao, V. Fatemi, S. Fang, K. Watanabe, T. Taniguchi, E. Kaxiras, P. Jarillo-Herrero, Unconventional superconductivity in magic-angle graphene superlattices. *Nature* **556**, 43–50 (2018).
2. W.-M. Zhao, L. Zhu, Z. Nie, Q.-Y. Li, Q.-W. Wang, L.-G. Dou, J.-G. Hu, L. Xian, S. Meng, S.-C. Li, Moiré enhanced charge density wave state in twisted 1T-$TiTe_2$/1T-$TiSe_2$ heterostructures. *Nat. Mater.* **21**, 284–289 (2021).
3. C. Jin, Z. Tao, T. Li, Y. Xu, Y. Tang, J. Zhu, S. Liu, K. Watanabe, T. Taniguchi, J. C. Hone, L. Fu, J. Shan, K. F. Mak, Stripe phases in WSe_2/WS_2 moiré superlattices. *Nat. Mater.* **20**, 940–944 (2021).
4. Y. Cao, V. Fatemi, A. Demir, S. Fang, S. L. Tomarken, J. Y. Luo, J. D. Sanchez-Yamagishi, K. Watanabe, T. Taniguchi, E. Kaxiras, R. C. Ashoori, P. Jarillo-Herrero, Correlated insulator behaviour at half-filling in magic-angle graphene superlattices. *Nature* **556**, 80–84 (2018).
5. Y. Xu, S. Liu, D. A. Rhodes, K. Watanabe, T. Taniguchi, J. Hone, V. Elser, K. F. Mak, J. Shan, Correlated insulating states at fractional fillings of moiré superlattices. *Nature* **587**, 214–218 (2020).
6. E. C. Regan, D. Wang, C. Jin, M. I. B. Utama, B. Gao, X. Wei, S. Zhao, W. Zhao, Z. Zhang, K. Yumigeta, M. Blei, J. D. Carlström, K. Watanabe, T. Taniguchi, S. Tongay, M. Crommie, A. Zettl, F. Wang, Mott and generalized Wigner crystal states in WSe_2/WS_2 moiré superlattices. *Nature* **579**, 359–363 (2020).
7. K. L. Seyler, P. Rivera, H. Yu, N. P. Wilson, E. L. Ray, D. G. Mandrus, J. Yan, W. Yao, X. Xu, Signatures of moiré-trapped valley excitons in $MoSe_2$/WSe_2 heterobilayers. *Nature* **567**, 66–70 (2019).
8. E. M. Alexeev, D. A. Ruiz-Tijerina, M. Danovich, M. J. Hamer, D. J. Terry, P. K. Nayak, S. Ahn, S. Pak, J. Lee, J. I. Sohn, M. R. Molas, M. Koperski, K. Watanabe, T. Taniguchi, K. S. Novoselov, R. V. Gorbachev, H. S. Shin, V. I. Fal'ko, A. I. Tartakovskii, Resonantly hybridized excitons in moiré superlattices in van der Waals heterostructures. *Nature* **567**, 81–86 (2019).
9. C. Jin, E. C. Regan, A. Yan, M. I. B. Utama, D. Wang, S. Zhao, Y. Qin, S. Yang, Z. Zheng, S. Shi, K. Watanabe, T. Taniguchi, S. Tongay, A. Zettl, F. Wang, Observation of moiré excitons in WSe_2/WS_2 heterostructure superlattices. *Nature* **567**, 76–80 (2019).
10. K. Tran, G. Moody, F. Wu, X. Lu, J. Choi, K. Kim, A. Rai, D. A. Sanchez, J. Quan, A. Singh, J. Embley, A. Zepeda, M. Campbell, T. Autry, T. Taniguchi, K. Watanabe, N. Lu, S. K. Banerjee, K. L. Silverman, S. Kim, E. Tutuc, L. Yang, A. H. MacDonald, X. Li, Evidence for moiré excitons in van der Waals heterostructures. *Nature* **567**, 71–75 (2019).
11. H. Yu, G.-B. Liu, J. Tang, X. Xu, W. Yao, Moiré excitons: From programmable quantum emitter arrays to spin-orbit–coupled artificial lattices. *Sci. Adv.* **3**, e1701696 (2017).
12. A. Ciarrocchi, F. Tagarelli, A. Avsar, A. Kis, Excitonic devices with van der Waals heterostructures: Valleytronics meets twistronics. *Nat. Rev. Mater.* **7**, 449–464 (2022).
13. L. Pitaevskii, S. Stringari, *Bose-Einstein Condensation and Superfluidity* (Oxford Univ. Press, 2016), vol. 164.
14. M. H. Anderson, J. R. Ensher, M. R. Matthews, C. E. Wieman, E. A. Cornell, Observation of Bose-Einstein condensation in a dilute atomic vapor. *Science* **269**, 198–201 (1995).
15. M. M. Fogler, L. V. Butov, K. S. Novoselov, High-temperature superfluidity with indirect excitons in van der Waals heterostructures. *Nat. Commun.* **5**, 4555 (2014).
16. Z. Wang, D. A. Rhodes, K. Watanabe, T. Taniguchi, J. C. Hone, J. Shan, K. F. Mak, Evidence of high-temperature exciton condensation in two-dimensional atomic double layers. *Nature* **574**, 76–80 (2019).
17. K. Ulman, S. Y. Quek, Organic-2D material heterostructures: A promising platform for exciton condensation and multiplication. *Nano Lett.* **21**, 8888–8894 (2021).
18. D. Snoke, Spontaneous Bose coherence of excitons and polaritons. *Science* **298**, 1368–1372 (2002).
19. K. B. Davis, M.-O. Mewes, M. R. Andrews, N. J. van Druten, D. S. Durfee, D. Kurn, W. Ketterle, Bose-Einstein condensation in a gas of sodium atoms. *Phys. Rev. Lett.* **75**, 3969 (1995).
20. L. Butov, C. Lai, A. Ivanov, A. Gossard, D. Chemla, Towards Bose–Einstein condensation of excitons in potential traps. *Nature* **417**, 47–52 (2002).
21. L. Butov, A. Gossard, D. Chemla, Macroscopically ordered state in an exciton system. *Nature* **418**, 751–754 (2002).
22. H. Guo, X. Zhang, G. Lu, Shedding light on moiré excitons: A first-principles perspective. *Sci. Adv.* **6**, eabc5638 (2020).
23. Y. Bai, L. Zhou, J. Wang, W. Wu, L. J. McGilly, D. Halbertal, C. F. B. Lo, F. Liu, J. Ardelean, P. Rivera, N. R. Finney, X.-C. Yang, D. N. Basov, W. Yao, X. Xu, J. Hone, A. N. Pasupathy, X.-Y. Zhu, Excitons in strain-induced one-dimensional moiré potentials at transition metal dichalcogenide heterojunctions. *Nat. Mater.* **19**, 1068–1073 (2020).
24. H. Guo, X. Zhang, G. Lu, Moiré excitons in defective van der Waals heterostructures. *Proc. Natl. Acad. Sci. U.S.A* **118**, e2105468118 (2021).
25. L. Butov, Exciton condensation in coupled quantum wells. *Solid State Commun.* **127**, 89–98 (2003).
26. A. G. del Aguila, Y. Wong, X. Liu, A. Fieramosca, T. T. H. Do, M. Battiato, Q. Xiong, *Exciton Condensation in an Atomically-Thin MoS_2 Semiconductor* (2021); https://doi.org/10.21203/rs.3.rs-940264/v1.
27. Y.-M. Xie, C.-P. Zhang, J.-X. Hu, K. F. Mak, K. Law, Valley-polarized quantum anomalous hall state in moiré $MoTe_2$/WSe_2 heterobilayers. *Phys. Rev. Lett.* **128**, 026402 (2022).
28. M. Palummo, M. Bernardi, J. C. Grossman, Exciton radiative lifetimes in two-dimensional transition metal dichalcogenides. *Nano Lett.* **15**, 2794–2800 (2015).
29. D. Wang, N. Luo, W. Duan, X. Zou, High-temperature excitonic Bose-Einstein condensate in centrosymmetric two-dimensional semiconductors. *J. Phys. Chem. Lett.* **12**, 5479–5485 (2021).

Downloaded from https://www.science.org on December 19, 2025

30. F. Nilsson, F. Aryasetiawan, Effects of dynamical screening on the BCS-BEC crossover in double bilayer graphene: Density functional theory for exciton bilayers. *Phys. Rev. Mater.* **5**, L050801 (2021).
31. P. Rivera, J. R. Schaibley, A. M. Jones, J. S. Ross, S. Wu, G. Aivazian, P. Klement, K. Seyler, G. Clark, N. J. Ghimire, J. Yan, D. G. Mandrus, W. Yao, X. Xu, Observation of long-lived interlayer excitons in monolayer $MoSe_2$–WSe_2 heterostructures. *Nat. Commun.* **6**, 6242 (2015).
32. R. Long, O. V. Prezhdo, Quantum coherence facilitates efficient charge separation at a MoS_2/$MoSe_2$ van der Waals junction. *Nano Lett.* **16**, 1996–2003 (2016).
33. L. Li, R. Long, O. V. Prezhdo, Charge separation and recombination in two-dimensional MoS_2/WS_2: Time-domain ab initio modeling. *Chem. Mater.* **29**, 2466–2473 (2017).
34. Q. Zheng, W. Chu, C. Zhao, L. Zhang, H. Guo, Y. Wang, X. Jiang, J. Zhao, Ab initio nonadiabatic molecular dynamics investigations on the excited carriers in condensed matter systems. *Wiley Interdiscip. Rev. Comput. Mol. Sci.* **9**, e1411 (2019).
35. M. Bayindir, B. Tanatar, Bose-Einstein condensation in a two-dimensional, trapped, interacting gas. *Phys. Rev. A* **58**, 3134–3137 (1998).
36. A. Minguzzi, S. Conti, M. Tosi, The internal energy and condensate fraction of a trapped interacting Bose gas. *J. Phys. Condens. Matter* **9**, L33 (1997).
37. G. Kresse, J. Furthmüller, Efficient iterative schemes for ab initio total-energy calculations using a plane-wave basis set. *Phys. Rev. B* **54**, 11169–11186 (1996).
38. G. Kresse, J. Furthmüller, Efficiency of ab-initio total energy calculations for metals and semiconductors using a plane-wave basis set. *Comput. Mater. Sci.* **6**, 15–50 (1996).
39. J. P. Perdew, K. Burke, M. Ernzerhof, Generalized gradient approximation made simple. *Phys. Rev. Lett.* **77**, 3865–3868 (1996).
40. P. Blöchl, Projector augmented-wave method. *Phys. Rev. B* **50**, 17953–17979 (1994).
41. S. Grimme, Semiempirical GGA-type density functional constructed with a long-range dispersion correction. *J. Comput. Chem.* **27**, 1787–1799 (2006).
42. E. Gross, W. Kohn, Local density-functional theory of frequency-dependent linear response. *Phys. Rev. Lett.* **55**, 2850 (1985).
43. M. A. Marques, N. T. Maitra, F. M. Nogueira, E. K. Gross, A. Rubio, *Fundamentals of Time-Dependent Density Functional Theory* (Springer Science & Business Media, 2012), vol. 837.
44. J. Liu, Z. Li, X. Zhang, G. Lu, Unraveling energy and charge transfer in type-II van der Waals heterostructures. *npj Comput. Mater.* **7**, 191 (2021).
45. L. Zhang, X. Zhang, G. Lu, One-dimensional flat bands and anisotropic moiré excitons in twisted tin sulfide bilayers. *Chem. Mater.* **33**, 7432–7440 (2021).
46. J. Liu, X. Zhang, G. Lu, Excitonic effect drives ultrafast dynamics in van der Waals heterostructures. *Nano Lett.* **20**, 4631–4637 (2020).
47. L.-y. Huang, X. Zhang, M. Zhang, G. Lu, Effect of point defects on optical properties of graphene fluoride: A first-principles study. *J. Phys. Chem. C* **121**, 12855–12862 (2017).
48. S. Refaely-Abramson, M. Jain, S. Sharifzadeh, J. B. Neaton, L. Kronik, Solid-state optical absorption from optimally tuned time-dependent range-separated hybrid density functional theory. *Phys. Rev. B* **92**, 081204 (2015).
49. S. Refaely-Abramson, S. Sharifzadeh, M. Jain, R. Baer, J. B. Neaton, L. Kronik, Gap renormalization of molecular crystals from density-functional theory. *Phys. Rev. B* **88**, 081204 (2013).
50. D. Wing, J. B. Haber, R. Noff, B. Barker, D. A. Egger, A. Ramasubramaniam, S. G. Louie, J. B. Neaton, L. Kronik, Comparing time-dependent density functional theory with many-body perturbation theory for semiconductors: Screened range-separated hybrids and the ***GW*** plus Bethe-Salpeter approach. *Phys. Rev. Mater.* **3**, 064603 (2019).
51. S. Refaely-Abramson, S. Sharifzadeh, N. Govind, J. Autschbach, J. B. Neaton, R. Baer, L. Kronik, Quasiparticle spectra from a nonempirical optimally tuned range-separated hybrid density functional. *Phys. Rev. Lett.* **109**, 226405 (2012).
52. L. Kronik, J. B. Neaton, Excited-state properties of molecular solids from first principles. *Annu. Rev. Phys. Chem.* **67**, 587–616 (2016).
53. J. Sun, C. A. Ullrich, Optical properties of $CsCu_2X_3$ (X= Cl, Br, and I): A comparative study between hybrid time-dependent density-functional theory and the Bethe-Salpeter equation. *Phys. Rev. Mater.* **4**, 095402 (2020).
54. A. Tal, P. Liu, G. Kresse, A. Pasquarello, Accurate optical spectra through time-dependent density functional theory based on screening-dependent hybrid functionals. *Phys. Rev. Res.* **2**, 032019 (2020).
55. Z.-h. Yang, F. Sottile, C. A. Ullrich, Simple screened exact-exchange approach for excitonic properties in solids. *Phys. Rev. B* **92**, 035202 (2015).
56. M. E. Casida, *Recent Advances in Density Functional Methods*, D. P. Chong, Ed. (World Scientific, 1995), vol. 1.
57. X. Zhang, Z. Li, G. Lu, First-principles simulations of exciton diffusion in organic semiconductors. *Phys. Rev. B* **84**, 235208 (2011).
58. T. Yamaoka, H. E. Lim, S. Koirala, X. Wang, K. Shinokita, M. Maruyama, S. Okada, Y. Miyauchi, K. Matsuda, Efficient photocarrier transfer and effective photoluminescence enhancement in type I monolayer $MoTe_2$/WSe_2 heterostructure. *Adv. Funct. Mater.* **28**, 1801021 (2018).
59. L. Wu, Y. Chen, H. Zhou, H. Zhu, Ultrafast energy transfer of both bright and dark excitons in 2D van der Waals heterostructures beyond dipolar coupling. *ACS Nano* **13**, 2341–2348 (2019).
60. J. Yang, T. Lu, Y. W. Myint, J. Pei, D. Macdonald, J.-C. Zheng, Y. Lu, Robust excitons and trions in monolayer $MoTe_2$. *ACS Nano* **9**, 6603–6609 (2015).
61. M. H. Naik, E. C. Regan, Z. Zhang, Y.-h. Chan, Z. Li, D. Wang, Y. Yoon, C. S. Ong, W. Zhao, S. Zhao, Nature of novel moiré exciton states in WSe_2/WS_2 heterobilayers. arXiv:2201.02562 [cond-mat.mes-hall] (2022).
62. H.-Y. Chen, V. A. Jhalani, M. Palummo, M. Bernardi, Ab initio calculations of exciton radiative lifetimes in bulk crystals, nanostructures, and molecules. *Phys. Rev. B* **100**, 075135 (2019).

Acknowledgments

Funding: This work was supported by the NSF-PREM program (DMR1828019) and the Army Research Office (W911NF-20-10305). **Author contributions:** G.L. designed the study, and H.G. carried out calculations with the assistance of X.Z. G.L. supervised the research and wrote the manuscript with H.G. All authors discussed the results. **Competing interests:** The authors declare that they have no competing interests. **Data and materials availability:** All data needed to evaluate the conclusions in the paper are present in the paper and/or the Supplementary Materials.

Submitted 9 March 2022
Accepted 22 August 2022
Published 7 October 2022
10.1126/sciadv.abp9757

Downloaded from https://www.science.org on December 19, 2025